Research Article

Samia Elattar, Umair Khan*, Aurang Zaib, Anuar Ishak, Norah Alwadai, and Ahmed M. Abed

Heat transfer characteristics of cobalt ferrite nanoparticles scattered in sodium alginate-based non-Newtonian nanofluid over a stretching/shrinking horizontal plane surface

https://doi.org/10.1515/phys-2023-0182
received November 08, 2023; accepted January 04, 2024

Abstract: Magnetite and cobalt ferrite ($CoFe_2O_4$) nanoparticles are frequently utilized in several applications, including magnetic drug delivery, hyperthermia, magnetic resonance imaging, *etc*. In the current investigation, the magnetohydrodynamic three-dimensional heat transfer (HT) flow induced by a non-Newtonian Eyring–Powell fluid is incorporated by a carrier sodium alginate ($NAC_6H_7O_6$)-based $CoFe_2O_4$ nanoparticles over a deformable (stretching/shrinking) horizontal plane surface with orthogonal shear stress and power-law velocity. The HT analysis along with the substantial effect of irregular heat source/sink as well as entropy generation is also performed. The similarity variables altered the posited leading equations into ordinary differential (similarity) equations. The function bvp4c in Matlab is then used to solve these equations numerically for various parameter values. Results indicate that, in general, there are two alternative solutions for the phenomenon of suction and deformable parameters. In addition, the essential thermal evaluation is enhanced owing to the significance of $CoFe_2O_4$ nanoparticles, magnetic parameter, and irregular heat source/sink.

Keywords: Eyring–Powell fluid, nanofluid, irregular heat source/sink, stretching/shrinking sheet, dual solutions

*** Corresponding author: Umair Khan,** Department of Mathematical Sciences, Faculty of Science and Technology, Universiti Kebangsaan Malaysia, UKM, Bangi, 43600, Selangor, Malaysia; Department of Mathematics, Faculty of Science, Sakarya University, Serdivan/Sakarya, 54050, Turkey; Department of Computer Science and Mathematics, Lebanese American University, Byblos, Lebanon, e-mail: umair.khan@lau.edu.lb, umairkhan@sakarya.edu.tr
Samia Elattar: Department of Industrial & Systems Engineering, College of Engineering, Princess Nourah bint Abdulrahman University, P.O. Box 84428, Riyadh, 11671, Saudi Arabia, e-mail: saelattar@pnu.edu.sa
Aurang Zaib: Department of Mathematical Sciences, Federal Urdu University of Arts, Science & Technology, Gulshan-e-Iqbal, Karachi-75300, Pakistan, e-mail: aurangzaib@fuuast.edu.pk
Anuar Ishak: Department of Mathematical Sciences, Faculty of Science and Technology, Universiti Kebangsaan Malaysia, UKM, Bangi, 43600, Selangor, Malaysia, e-mail: anuar_mi@ukm.edu.my
Norah Alwadai: Department of Physics, College of Science, Princess Nourah bint Abdulrehman University, P.O. Box 84428, Riyadh, 11671, Saudi Arabia, e-mail: nmalwadai@pnu.edu.sa
Ahmed M. Abed: Department of Industrial Engineering, College of Engineering, Prince Sattam bin Abdulaziz University, Alkharj, 16273, Saudi Arabia, e-mail: a.abed@psau.edu.sa

1 Introduction

Nanofluids (NFs) are being used in industrial and scientific processes. They make up a distinct group of nanomaterials. Compared to metals, liquids used for heat transfer (HT), such as water, engine oil, and ethylene glycol, have low thermal conductivity. A considerable increase in heat conduction can therefore be achieved by distributing solid metal particles in heat diffusion [1]. The effects of slip on the 2D flow of an NF past an axisymmetric stretchable sheet with suction were scrutinized by Gorder *et al.* [2]. Das [3] discovered the performance of convective heat transport (CHT) incorporated NF *via* a porous stretched sheet with impacts of slip and heat absorption/generation. Water-based copper and alumina nanoparticles are considered to simulate the behavior of HT fluid flow. Noghrehabadi *et al.* [4] studied a computational simulation of the NF flow across a porous stretchable cylinder and utilized a two-phase model subject to a magnetic field (MF). The magnetohydrodynamic (MHD) time-dependent free convective flow of water-based dissimilar nanoparticles toward a vertical permeable stretchable surface was examined by Freidoonimehr *et al.* [5]. Naramgari and Sulochana [6] investigated the MHD NF flow across an exponential stretching sheet in a porous media. The impacts of heat generation/absorption and thermal radiation were included in this scrutiny. The investigation concluded that the exponential parameter enhances the effects of mass and HT.

Makinde *et al.* [7] calculated the impression of MHD on the NF flow across an irregular stretchy sheet with a chemical reaction. The impact of heat sinks/sources as well as radiation was presented to talk about the flow behavior. Acharya *et al.* [8] highlighted the characteristics of Hall current on the MHD hybrid NFs flow through a rotatable disc due to thermal radiation. From the analysis, it is exposed that the HT uplifts for the radiative parameter and the temperature decreases for the Hall parameter. Zaib *et al.* [9] inspected the buoyancy flow and heat transport progression incorporated micropolar NF across a wedge. They found that dual solutions exist in the opposing flow case only. Recently, Khan *et al.* [10] surveyed the influence of radiation on a buoyancy flow caused by an NF *via* a stretchable porous bent sheet. The slip migration, binary reaction, and activation energy are all taken into consideration to explore the specifics of water-based Al_2O_3 nanoparticles. Recently, Divya *et al.* [11] considered the influence of suction/injection on the radiative flow and HT of NF past a Riga plate with heat source/sink and Cattaneo–Christov model. They found that the velocity and the temperature declined owing to suction.

A subclass of NFs known as magnetic NFs (MNFs) is made up of colloidal suspensions of nanoscale magnetic particles that exhibit both magnetic and fluid properties. These particles are typically 5–10 nm in size. Magnetic nanoparticles are typically synthesized from metals and their oxides, such as Mn–Zn ferrite, cobalt ferrite ($CoFe_2O_4$), and iron oxide, in either polar or non-polar fluid transporters, including oil, water, and ethylene glycol in a range of shapes and sizes. The capacity of MNFs to quickly change viscosity is its main advantage [12]. A variety of applications for magnetic nanoparticles have a great deal of potential due to their special material characteristics. Magnetic nanoparticles are particularly appealing for biological applications due to their physiochemical features, including a large surface area-to-volume ratio and the possibility of surface functioning [13]. They are intriguing substances with numerous uses, such as magnetic separation, biosensors, magnetic resonance imaging, targeted drug delivery, HT/dissipation, magneto-optic sensors, *etc*. Khan *et al.* [14] observed the characteristics of the HT and SPF of $CoFe_2O_4$ nanoparticles with viscous dissipation toward a stretchable sheet. They professed that the profile of temperature reduces due to magnetic and Eckert numbers. The enhancement of HT by utilizing a non-Newtonian fluid through sodium alginate ($NAC_6H_7O_6$)-based non-magnetic and magnetic particles was explored by Hussanan *et al.* [15]. Joshi *et al.* [16] assessed the influence of the high-order chemical reaction on the magneto flow of water-based hybrid NFs across a permeable bidirectional stretched sheet with volumetric heat generation. The results obtained from the current problem show that the thermal profile grows as the volume fraction increases, while the velocity decreases. The characteristic of magnetic flow induced by hybrid NFs past a stretchable sheet with the mechanism of slip effect was inspected by Pandey *et al.* [17]. They observed that the velocity augments due to the free convective parameter. Tadesse *et al.* [18] investigated the 2D Darcy–Forchheimer flow (DFF) toward a stagnation point past a shrinkable sheet induced by magnetic ferrofluids with convective heating and dissipation effects. The findings suggest that there are two possible solutions for the shrinking sheet. Tshivhi and Makinde [19] explored the influence of MF on the flow and coolant HT made of NF across a heated movable sheet. It is discovered that there are dual solutions within a particular range of shrinking sheets. Shafiq *et al.* [20] discussed the impression of erratic radiation on the DFF and HT incorporated by $CoFe_2O_4$ Casson fluid past a rotatable stretched sheet. Usman *et al.* [21] examined the water-based $CoFe_2O_4$ and copper nanoparticles by considering the theory of Darcy–Forchheimer through an exponentially stretched sheet with radiation effect. The nonlinear heat source/sink effects on an unsteady flow through a deformable sheet induced by water-based $CoFe_2O_4$ nanoparticles with porous media were scrutinized by Waini *et al.* [22]. Dual solutions are found for a particular strength of the shrinking parameter along with the unsteady parameter. Tshivhi and Makinde [23] examined the combined impact of Joule heating and MF on the dissipative flow of NF across a slippery and shrinking surface and obtained dual solutions. The stability analysis is also performed to check the stable solution and found that the upper solution is stable, whereas the lower solution is unstable. Recently, Murtaza *et al.* [24] explored the significance of $CoFe_2O_4$ nanoparticles through irregular viscosity and second-order slip past an extendable sheet in a porous media.

For a more extensive understanding of engineering and manufacturing technology issues, it is crucial to take into account research on boundary layer phenomena that focus on non-Newtonian heat-transfer substances. These substances advance widely during many industrial processes, including missile guidance, fluidization, nuclear reactor cooling, rain erosion, aerosol, and paint spraying. Although the existence of such substances is extremely problematic, numerous fundamental models/problems have been created and investigated to determine the proper flow behavior. One of the subclasses of the non-Newtonian fluid models is the Eyring–Powell fluid (EPF) model. As opposed to other non-Newtonian fluids, the model of EPF has a substantial advantage because, in place of empirical relations, it is derived from the key theory known as the "kinetic theory of gases." More importantly, it advances at high shear rates as a viscous fluid [25]. The subject of EPF

across a constantly movable porous surface with a parallel free stream has been addressed by Jalil *et al.* [26]. Hayat *et al.* [27] explored the significance of convective boundary conditions (BCs) on the flow and HT induced by EPF across a movable surface with a stable free stream. They presented an analytic solution. The features of fluid flow and thermal transport across a shrinkable surface were investigated by Roşca and Pop [28]. They performed the stability analysis to find a stable solution. Rahimi *et al.* [29] studied the viscous flow of a non-Newtonian EPF across a stretchable sheet and exploited the collocation technique to acquire the posited outcome. It is observed that raising the fluid material parameter causes the velocity to drop while expanding the EPF material parameter causes it to increase. Reddy *et al.* [30] reviewed the impression of chemical reaction on the MHD flow of EPF past a stretching slandering sheet with solar energy, solutal, thermal, and velocity slips. It has been observed that larger values of radiative HT have a greater impact on the temperature. Abbas and Megahed [31] explored the influence of radiation on the dissipative flow of EPF past a stratified surface in a porous media and obtained a numerical solution by the Chebyshev spectral technique. It is demonstrated that the temperature profile is dramatically impacted by the existence of viscous dissipation and thermal radiation in the fluid flow. Recently, Aljabali *et al.* [32] investigated the relationship between the motions of dusty scale particles under the impact of buoyancy convective flow of EPF. The finding suggests that the particles of dusty have an influence on fluid motion, which caused a slowdown in fluid transmission.

The current study uses a model developed by Tiwari and Das [33] to investigate the EPF flow of $NAC_6H_7O_6$ (sodium alginate)-based $CoFe_2O_4$ NF *via* a deformable (stretchable/shrinkable) horizontal plane surface (DHPS). To fully understand the nuances of NF flow, irregular heat source/sink and magnetic effects are also accomplished. The modified system of ordinary differential equations is obtained using the similarity parameters, and it is then numerically determined using the bvp4c. In this examination, bifurcation values for the substantial constraints are also presented. The attained bifurcation values are renowned as the value at which laminar boundary-layer flow (BLF) separates from turbulent BLF. Since, the non-unique solutions or dual solutions frequently occurred due to the case of the shrinking/stretching sheet, the mass transpiration velocity and the posited unconfined vorticity inside the boundary layer. As a result, when the key outcome rate is reached, operations for some items can be designed to produce the required results, and productivity will be optimized. Therefore, it is advantageous to investigate the sodium alginate-based $CoFe_2O_4$ nanomaterials with EPF, including the controlling factors that can slow the process of flow separation and speed up the rate of HT. This endeavor is important because it will serve as a future resource for engineers, fluid mechanics experts, scientists, and practitioners. It will also serve as a foundational analysis for actual applications.

2 Mathematical formulation of the problem

Let us consider the three-dimensional incompressible MHD EPF (non-Newtonian) model with HT characteristics conveying $CoFe_2O_4$ nanoparticles in a regular $NAC_6H_7O_6$-based fluid over a DHPS subjected to irregular heat source/sink and suction effects. The following equations guide the EPF model:

$$\operatorname{div} \mathbf{V} = 0, \tag{1}$$

$$\rho_{\mathrm{nf}} \frac{\mathrm{D}\mathbf{V}}{\mathrm{D}t} = -\nabla \mathbf{p} + \operatorname{div}\mathbf{S}, \tag{2}$$

where $\mathbf{V}$ signifies the velocity vector field, ρ_{nf} indicates the NF density, $\frac{\mathrm{D}}{\mathrm{D}t}$ represents the operator for the material time derivative, $\mathbf{p}$ represents the NF pressure, and $\mathbf{S}$ stands for the tensor of Cauchy stress. It is indicated that the constitutive equation for the NF model of EPF is as follows [34]:

$$\mathbf{S} = \mu_{\mathrm{nf}} \nabla \mathbf{V} + \frac{1}{\beta_{\mathrm{b}}} \operatorname{Sinh}^{-1}\left(\frac{1}{\delta_{\mathrm{b}}} \nabla \mathbf{V}\right). \tag{3}$$

The final term on the right-hand side of Eq. (3) can be expressed as [34], which is the second-order estimation of the function:

$$\sinh^{-1}\left(\frac{1}{\delta_{\mathrm{b}}} \nabla \mathbf{V}\right) \approx \left[\frac{1}{\delta_{\mathrm{b}}} \nabla \mathbf{V} - \frac{1}{6}\left(\frac{1}{\delta_{\mathrm{b}}} \nabla V\right)^3\right], \quad \left|\frac{1}{\delta_{\mathrm{b}}} \nabla \mathbf{V}\right| \ll 1, \tag{4}$$

where μ_{nf} is the viscosity of the NF, and β_{b} and δ_{b} signify the material constants of the EPF model. The physical configuration of the non-Newtonian three-dimensional flow problem is exposed in Figure 1, where the geometry is designed *via* the Cartesian coordinate system x_{b}, y_{b}, and z_{b}, which is used with corresponding velocities u_{b}, v_{b}, and w_{b}. Here, x_{b} – axis and y_{b} – axis coordinates are reserved literally for the respective SMW (streamwise) and SNW (spanwise) directions, while the z_{b} – axis is perpendicular to the DHPS. Assume that the velocities of both SMW and SNW at the HPS (horizontal plane surface) are represented by $u_{\mathrm{wb}}(x_{\mathrm{b}}) = Ax_{\mathrm{b}}^m$ and $v_{\mathrm{wb}}(x_{\mathrm{b}}) = Bx_{\mathrm{b}}^m$, in which, A, B resemble the stretching rates [35] in the corresponding x_{b} – and y_{b} – directions. Moreover, $w_{\mathrm{b}}(x_{\mathrm{b}}) = w_0$ corresponds the suction/injection velocity with $w_0 < 0$, and $w_0 > 0$ represent the cases of injection and suction, respectively, whereas the impermeable

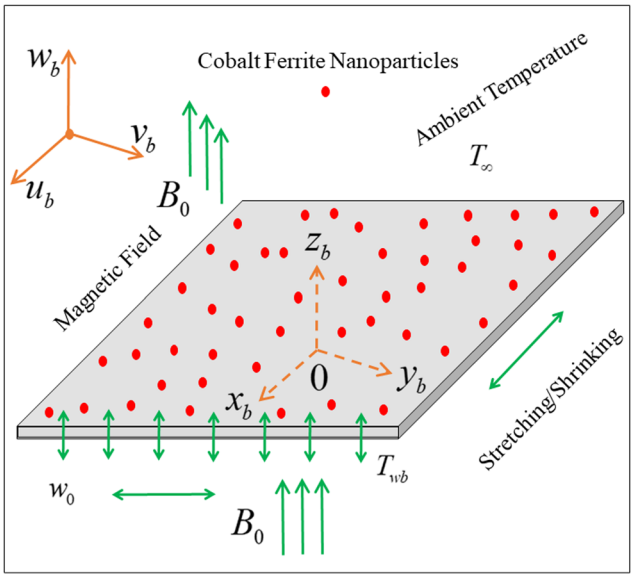

Figure 1: Physical model and Cartesian coordinates.

HPS is represented by $w_0 = 0$. Also, it is assumed that the constant temperature located in the HPS and ambient temperature are referred to the corresponding notations such as T_{wb} and T_∞. A constant MF B_0 is applied normal to the HPS. The magnetic Reynolds number is treated as a very small quantity to ignore the induced MF. For thermal improvement, the $CoFe_2O_4$ nanoparticle is considered into the regular-based (sodium alginate) fluid to form the requisite NF.

With the help of the above-stated assumptions and the boundary layer approximations, the main simplified equations in terms of PDEs of the NF can be written as follows [32,34]:

$$\frac{\partial u_b}{\partial x_b} + \frac{\partial v_b}{\partial y_b} + \frac{\partial w_b}{\partial z_b} = 0, \tag{5}$$

$$\rho_{nf}\left(u_b\frac{\partial u_b}{\partial x_b} + v_b\frac{\partial u_b}{\partial y_b} + w_b\frac{\partial u_b}{\partial z_b}\right) = \left(\mu_{nf} + \frac{1}{\beta_b\delta_b}\right)\frac{\partial^2 u_b}{\partial z_b^2} - \frac{1}{2\beta_b\delta_b{}^3}\left(\frac{\partial u_b}{\partial z_b}\right)^2\frac{\partial^2 u_b}{\partial z_b^2} - \sigma_{nf}B_0^2 u_b, \tag{6}$$

$$\rho_{nf}\left(u_b\frac{\partial v_b}{\partial x_b} + v_b\frac{\partial v_b}{\partial y_b} + w_b\frac{\partial v_b}{\partial z_b}\right) = \left(\mu_{nf} + \frac{1}{\beta_b\delta_b}\right)\frac{\partial^2 v_b}{\partial z_b^2} - \frac{1}{2\beta_b\delta_b{}^3}\left(\frac{\partial v_b}{\partial z_b}\right)^2\frac{\partial^2 v_b}{\partial z_b^2} - \sigma_{nf}B_0^2 v_b, \tag{7}$$

$$(\rho c_p)_{nf}\left(u_b\frac{\partial T_b}{\partial x_b} + v_b\frac{\partial T_b}{\partial y_b} + w_b\frac{\partial T_b}{\partial z_b}\right) = k_{nf}\frac{\partial^2 T_b}{\partial z_b^2} + \frac{k_{nf}u_{wb}(x_b)}{x_b\nu_{nf}}[A_c^*(T_{wb} - T_\infty)e^{-\xi} + B_c^*(T_b - T_\infty)], \tag{8}$$

subject to the following physical BCs are

$$u_b = \gamma_c u_{wb}(x_b),\ v_b = \gamma_c v_{wb}(x_b),\ w_b = w_0,\ T_b = T_{wb} \text{ at } z_b = 0,$$
$$u_b \to 0,\ v_b \to 0,\ T_b \to T_\infty \text{ as } z_b \to \infty. \tag{9}$$

Here, δ_b and β_b refer to the EPF or material constraints, T_b is the temperature of the NF, A_c^* denotes the "exponentially decaying space coefficients," and B_c^* is called the "time-dependent heat absorption/generation." Additionally, the negative and positive simultaneous values of A_c^* and B_c^* formed the posited phenomena of heat sink and heat source, respectively. Therefore, the DHPS is denoted by γ_c with $\gamma_c > 0$ for "stretching case," and $\gamma_c < 0$ for "shrinking case" while the case $\gamma_c = 0$ represents the static HPS.

In addition, the lasting mathematical notations used in the aforesaid equations for the thermophysical properties (TPPs) of the NF are σ_{nf} the "electrical conductivity," ρ_{nf} the "density," k_{nf} the "TCN," μ_{nf} the "viscosity," and $(\rho c_p)_{nf}$ the "specific heat." Hence, Table 1 shows the relationships of these TPPs of the NF.

Furthermore, the symbol φ_{sc} parades the solid nanoparticle volume fraction. However, the specific condition $\varphi_{sc} = 0$ reduces the equations of the NF model into a carrier-based $NAC_6H_7O_6$ (sodium alginate) fluid. Likewise, the subscript notations like nf, s_c, and f, respectively, called the NF, nanoparticles, and the carrier-based $NAC_6H_7O_6$ fluid. However, c_p refers to the requisite posited "heat capacitance at uniform pressure." The experimentation data set of the regular base $NAC_6H_7O_6$ fluid and the $CoFe_2O_4$ are quantitatively mentioned in Table 2.

To comfort the scrutinization of the model, therefore, we posit a similarity ansatz satisfying the above "continuity equation" (5) as follows:

Table 1: Requisite posited correlations of $NAC_6H_7O_6$-based $CoFe_2O_4$ nanoparticles [18,19,36]

Properties	NF correlations
Absolute viscosity	$\mu_{nf} = \mu_f(1-\varphi_{sc})^{-2.5}$
Density	$\rho_{nf} = \rho_f\left[\varphi_{sc}\left(\frac{\rho_{sc}}{\rho_f}\right) + (1-\varphi_{sc})\right]$
Heat capacity	$(\rho c_p)_{nf} = (\rho c_p)_f\left[\varphi_{sc}\left(\frac{(\rho c_p)_{sc}}{(\rho c_p)_p}\right) + (1-\varphi_{sc})\right]$
Thermal conductivity	$k_{nf} = k_f\left[\frac{(k_{sc}+2k_f) - 2\varphi_{sc}(k_f - k_{sc})}{(k_{sc}+2k_f) + \varphi_{sc}(k_f - k_{sc})}\right]$
Electrical conductivity	$\sigma_{nf} = \sigma_f\left[1 + \frac{3\left(\frac{\sigma_s}{\sigma_f} - 1\right)}{\left(\frac{\sigma_s}{\sigma_f}+2\right) - \left(\frac{\sigma_s}{\sigma_f} - 1\right)\varphi_{sc}}\right]$

Table 2: TPPs of the $NAC_6H_7O_6$-based fluid and the $CoFe_2O_4$ nanoparticles [37,38]

Properties	ρ(kg/m^3)	c_p (J/kg K)	k (W/m K)	σ (S/m)	Pr
$NAC_6H_7O_6$	989	4,175	0.6376	2.60×10^{-4}	6.45
$CoFe_2O_4$	4,907	700	3.7	1.1×10^{7}	

$$u_b = Ax_b^m F'(\xi),\ v_b = Bx_b^m G'(\xi),\ \xi = (A/\upsilon_f)^{1/2} C(x_b) z_b,$$
$$w_b = -\frac{\sqrt{A\upsilon_f}}{C}\left[mx_b^{m-1}F(\xi) + x_b^m \frac{C_{x_b}}{C}\{\xi F'(\xi) - F(\xi)\}\right], \tag{10}$$

where ξ refers to the "pseudo-similarity variable" and a prime indicates the differentiation by variable ξ. Also, $C = C(x_b)$ and $C_{x_b} = \frac{dC(x_b)}{dx_b}$. Using Eq. (10), the SMW and SNW Eqs. (6) and (7) for momentum are changed into the following reduced form as follows:

$$\frac{\rho_f}{\rho_{nf}}\left(\frac{\mu_{nf}}{\mu_f} + \frac{1}{\beta_b \delta_b \mu_f}\right) C^2 F''' - \frac{\rho_f}{\rho_{nf}} \frac{A^3 x_b^{2m} C^4}{2\beta_b \delta_b{}^3 \mu_f \upsilon_f} F''^2 F''' - \left(\frac{\sigma_{nf}/\sigma_f}{\rho_{nf}/\rho_f}\right)\frac{\sigma_f B_0^2}{\rho_f A} F' + \left(mx_b^{m-1} - \frac{C_{x_b}}{C} x_b^m\right) FF'' - mx_b^{m-1} F'^2 = 0, \tag{11}$$

$$\frac{\rho_f}{\rho_{nf}}\left(\frac{\mu_{nf}}{\mu_f} + \frac{1}{\beta_b \delta_b \mu_f}\right) C^2 G''' - \frac{\rho_f}{\rho_{nf}} \frac{AB^2 x_b^{2m} C^4}{2\beta_b \delta_b{}^3 \mu_f \upsilon_f} G''^2 G''' - \left(\frac{\sigma_{nf}/\sigma_f}{\rho_{nf}/\rho_f}\right)\frac{\sigma_f B_0^2}{\rho_f A} G' + \left(mx_b^{m-1} - \frac{C_{x_b}}{C} x_b^m\right) FG'' - mx_b^{m-1} F'G' = 0. \tag{12}$$

To obtain the similarity equations (see Weidman [35] and Khan *et al.* [39]), the following term was adopted as follows:

$$\frac{C_{x_b}}{C} = \frac{K_c m}{x_b}. \tag{13}$$

Now, using integration by parts, we obtain

$$C = D_c x_b^{K_c m}, \tag{14}$$

where D_c and K_c are requisite arbitrary constants. In addition, we put $\beta_b = \beta_c x_b^{-\left(\frac{3m-1}{2}\right)}$, and $\delta_b = \delta_c x_b^{\frac{3m-1}{2}}$ function with constants EPF parameters β_c and δ_c, while $\sigma_f = \sigma_f^* x_b^{\frac{m-1}{2}}$ is the base fluid electrical conductivity which is assumed as a function of x_b that makes the momentum equations are dimensionless. Substituting Eqs. (13), (14), and the above functional parameters into both (SMW and SNW) Eqs. (11) and (12) yields

$$\frac{\rho_f}{\rho_{nf}}\left(\frac{\mu_{nf}}{\mu_f} + \frac{1}{\beta_c \delta_c \mu_f}\right) F''' - \frac{\rho_f}{\rho_{nf}} \frac{1}{2\beta_c \delta_c \mu_f} \frac{A^3 x_b^{2m} D_c{}^2 x_b^{2K_c m}}{\delta_c{}^2 x_b^{3m-1} \upsilon_f} F''^2 F''' - \left(\frac{\sigma_{nf}/\sigma_f}{\rho_{nf}/\rho_f}\right)\frac{\sigma_f^* B_0^2 x_b^{m-1}}{\rho_f A D_c{}^2 x_b^{2K_c m}} F' + \left(\frac{mx_b^{m-1} - K_c m x_b^{m-1}}{D_c{}^2 x_b^{2K_c m}}\right) FF'' - \frac{mx_b^{m-1}}{D_c{}^2 x_b^{2K_c m}} F'^2 = 0, \tag{15}$$

$$\frac{\rho_f}{\rho_{nf}}\left(\frac{\mu_{nf}}{\mu_f} + \frac{1}{\beta_c \delta_c \mu_f}\right) G''' - \frac{\rho_f}{\rho_{nf}} \frac{1}{2\beta_c \delta_c \mu_f} \frac{AB^2 x_b^{2m} D_c{}^2 x_b^{2K_c m}}{\delta_c{}^2 x_b^{3m-1} \upsilon_f} G''^2 G''' - \left(\frac{\sigma_{nf}/\sigma_f}{\rho_{nf}/\rho_f}\right)\frac{\sigma_f^* B_0^2 x_b^{m-1}}{\rho_f A D_c{}^2 x_b^{2K_c m}} G' + \left(\frac{mx_b^{m-1} - K_c m x_b^{m-1}}{D_c{}^2 x_b^{2K_c m}}\right) FG'' - \frac{mx_b^{m-1}}{D_c{}^2 x_b^{2K_c m}} G'F' = 0. \tag{16}$$

Thus, the coefficient of FF'' and the coefficient of FG'' are equally set to unity, so that,

$$D_c = \sqrt{\frac{m+1}{2}},\ \text{and}\ K_c = \frac{m-1}{2m}, \tag{17}$$

and Eqs. (15) and (16) become as follows:

$$\frac{1}{\rho_{nf}/\rho_f}\left(\frac{\mu_{nf}}{\mu_f} + \Sigma_a\right) F''' - \left(\frac{m+1}{4}\right)\frac{\Sigma_a \Sigma_b}{\rho_{nf}/\rho_f} F''^2 F''' + FF'' - \frac{2m}{m+1} F'^2 - \left(\frac{2}{m+1}\right)\frac{\sigma_{nf}/\sigma_f}{\rho_{nf}/\rho_f} M_c F' = 0, \tag{18}$$

$$\frac{1}{\rho_{nf}/\rho_f}\left(\frac{\mu_{nf}}{\mu_f} + \Sigma_a\right) G''' - \left(\frac{m+1}{4}\right)\frac{\Sigma_a \Sigma_b}{\rho_{nf}/\rho_f} E_c^2 G''^2 G''' + FG'' - \frac{2m}{m+1} F'G' - \left(\frac{2}{m+1}\right)\frac{\sigma_{nf}/\sigma_f}{\rho_{nf}/\rho_f} M_c G' = 0. \tag{19}$$

Moreover, the distinguished parameters in the dimensionless form are defined as follows: $\Sigma_a = \frac{1}{\beta_c \delta_c \mu_f}$ and $\Sigma_b = \frac{A^3}{\delta_c^2 \upsilon_f}$ the EPF parameter, $M_c = \frac{\sigma_f^* B_0^2}{\rho_f A}$ the magnetic parameter, and $E_c = \frac{B}{A}$ the stretching rate ratio parameter.

In addition, using Eq. (10) along with $S(\xi) = \frac{T_b - T_\infty}{T_{wb} - T_\infty}$, the energy Eq. (8) is changed to the following obligatory form:

$$\frac{C^2}{\mathrm{Pr}} \frac{k_{nf}/k_f}{(\rho c_p)_{nf}/(\rho c_p)_f} S'' + \left(mx_b^{m-1} - \frac{C_{x_b}}{C} x_b^m\right) FS' + \frac{1}{\mathrm{Pr}} \frac{(k_{nf}/k_f)(\rho_{nf}/\rho_f) x_b^{m-1}}{((\rho c_p)_{nf}/(\rho c_p)_f)(\mu_{nf}/\mu_f)} [A_c^* e^{-\xi} + B_c^* S] = 0. \tag{20}$$

Using Eqs. (13), (14), and (17), the same practice is followed to renovate Eq. (20), so that we obtain

$$\frac{k_{\mathrm{nf}}}{k_{\mathrm{f}}}S'' + \mathrm{Pr}\frac{(\rho c_{\mathrm{p}})_{\mathrm{nf}}}{(\rho c_{\mathrm{p}})_{\mathrm{f}}}FS' + \left(\frac{2}{m+1}\right)\frac{\left(\frac{\rho_{\mathrm{nf}}}{\rho_{\mathrm{f}}}\right)\left(\frac{k_{\mathrm{nf}}}{k_{\mathrm{f}}}\right)}{\left(\frac{\mu_{\mathrm{nf}}}{\mu_{\mathrm{f}}}\right)}[A_{\mathrm{c}}^{*}e^{-\xi} + B_{\mathrm{c}}^{*}S] = 0. \tag{21}$$

Furthermore, the suction/injection factor for the HPS is given by

$$w_0 = -\frac{\sqrt{Av_{\mathrm{f}}}}{C}\left(\frac{m+1}{2}\right)x_{\mathrm{b}}^{m-1}f_{\mathrm{wc}}, \tag{22}$$

and the changed BCs are

$$\begin{cases} G(0) = 0,\ F(0) = f_{\mathrm{wc}},\ G'(0) = F'(0) = \gamma_{\mathrm{c}},\ S(0) = 1, \\ G'(\xi) \to 0,\ F'(\xi) \to 0,\ S(\xi) \to 0 \text{as } \xi \to \infty, \end{cases} \tag{23}$$

where f_{wc} refers to the suction/injection factor with $f_{\mathrm{wc}} > 0$ refers to the case of suction and $f_{\mathrm{wc}} < 0$ refers to the case of injection, whereas $f_{\mathrm{wc}} = 0$ refers to the impermeable HFS. Also, the Prandtl number is represented by $\mathrm{Pr} = v_{\mathrm{f}}/\alpha_{\mathrm{f}}$.

In this examination, it is pointed ready that a given model is compacted to the "third extension of the Bank's problem" (see Weidman [35]); if $f_{\mathrm{wc}} = 0$ (impermeable surface), $M_{\mathrm{c}} = 0$ (without MF), $\gamma_{\mathrm{c}} = 1$ (stretching surface), $\Sigma_{\mathrm{a}} = 0$, $\Sigma_{\mathrm{b}} = 0$ (Newtonian model), and $\varphi_{\mathrm{s_c}} = 0$ (carrier-based fluid) are examined. However, Weidman [35] did not include the HT characteristics because the equation of energy was left out or omitted. In addition, due to the case of viscous fluid, with no effects of the MF, permeable flat plate and Newtonian model are considered, Eqs. (18) and (23) can also be simplified to Miklavčič and Wang [40] (linear shrinking) and Fang [41] (power-law shrinking). These published works also did not explore the requisite energy equation.

The gradients of engineering physical interests are the skin friction coefficient in the SMW (C_{f}), the skin friction coefficient in the SNW (C_{g}), and the local HT rate (HTR) $\mathrm{Nu}_{x_{\mathrm{b}}}$, which is defined as follows:

$$C_{\mathrm{f}} = \frac{1}{\rho_{\mathrm{f}}u_{\mathrm{wb}}^2}\left[\left(\mu_{\mathrm{nf}} + \frac{1}{\beta_{\mathrm{b}}\delta_{\mathrm{b}}}\right)\frac{\partial u_{\mathrm{b}}}{\partial z_{\mathrm{b}}} - \frac{1}{6\beta_{\mathrm{b}}\delta_{\mathrm{b}}^3}\left(\frac{\partial u_{\mathrm{b}}}{\partial z_{\mathrm{b}}}\right)^3\right]\Bigg|_{z_{\mathrm{b}}=0},$$

$$C_{\mathrm{g}} = \frac{1}{\rho_{\mathrm{f}}v_{\mathrm{wb}}^2}\left[\left(\mu_{\mathrm{nf}} + \frac{1}{\beta_{\mathrm{b}}\delta_{\mathrm{b}}}\right)\frac{\partial v_{\mathrm{b}}}{\partial z_{\mathrm{b}}} - \frac{1}{6\beta_{\mathrm{b}}\delta_{\mathrm{b}}^3}\left(\frac{\partial v_{\mathrm{b}}}{\partial z_{\mathrm{b}}}\right)^3\right]\Bigg|_{z_{\mathrm{b}}=0}, \tag{24}$$

and

$$\mathrm{Nu}_{x_{\mathrm{b}}} = \frac{x_{\mathrm{b}}}{k_{\mathrm{f}}(T_{wb} - T_{\infty})}\left(-k_{\mathrm{nf}}\frac{\partial T_{\mathrm{b}}}{\partial z_{\mathrm{b}}}\right)\Bigg|_{z_{\mathrm{b}}=0}.$$

Using (10), (13), (14), and (17) with $S(\xi) = \frac{T_{\mathrm{b}} - T_{\infty}}{T_{\mathrm{wb}} - T_{\infty}}$ into the aforementioned Eq. (24), the following obtained dimensionless form of the gradients takes place:

$$\mathrm{Re}_{x_{\mathrm{b}}x_{\mathrm{b}}}^{1/2}C_{\mathrm{f}} = \sqrt{\frac{m+1}{2}}\left[\left(\frac{\mu_{\mathrm{nf}}}{\mu_{\mathrm{f}}} + \Sigma_{\mathrm{a}}\right)F''(0) - \left(\frac{m+1}{12}\right)\Sigma_{\mathrm{a}}\Sigma_{\mathrm{b}}F''(0)^3\right],$$

$$\mathrm{Re}_{y_{\mathrm{b}}x_{\mathrm{b}}}^{1/2}C_{\mathrm{g}} = \sqrt{\frac{m+1}{2}}\frac{1}{\sqrt{E_{\mathrm{c}}}}\left[\left(\frac{\mu_{\mathrm{nf}}}{\mu_{\mathrm{f}}} + \Sigma_{a}\right)G''(0) - \left(\frac{m+1}{12}\right)E_{\mathrm{c}}^2\Sigma_{\mathrm{a}}\Sigma_{\mathrm{b}}G''(0)^3\right], \tag{25}$$

and

$$\mathrm{Re}_{x_{\mathrm{b}}x_{\mathrm{b}}}^{-1/2}\mathrm{Nu}_{x_{\mathrm{b}}} = -\sqrt{\frac{m+1}{2}}\frac{k_{\mathrm{nf}}}{k_{\mathrm{f}}}S'(0).$$

Hence, $\mathrm{Re}_{x_{\mathrm{b}}x_{\mathrm{b}}} = \frac{u_{\mathrm{wb}}(x_{\mathrm{b}})x_{\mathrm{b}}}{v_{\mathrm{f}}}$ and $\mathrm{Re}_{y_{\mathrm{b}}x_{\mathrm{b}}} = \frac{v_{\mathrm{wb}}(x_{\mathrm{b}})x_{\mathrm{b}}}{v_{\mathrm{f}}}$ are the local Reynolds number.

3 Entropy analysis

The expression of volumetric entropy generation induced by Eyring–Powell NF is given by

$$\mathrm{EG} = \frac{k_{\mathrm{nf}}}{T_{\infty}^2}\left(\frac{\partial T_{\mathrm{b}}}{\partial z_{\mathrm{b}}}\right)^2 + \frac{1}{T_{\infty}}\left[\left(\mu_{\mathrm{nf}} + \frac{1}{\beta_{\mathrm{b}}\delta_{\mathrm{b}}}\right)\left(\frac{\partial u_{\mathrm{b}}}{\partial z_{\mathrm{b}}} + \frac{\partial v_{\mathrm{b}}}{\partial z_{\mathrm{b}}}\right)^2 - \frac{1}{2\beta_{\mathrm{b}}\delta_{\mathrm{b}}^3}\left(\frac{\partial u_{\mathrm{b}}}{\partial z_{\mathrm{b}}} + \frac{\partial v_{\mathrm{b}}}{\partial z_{\mathrm{b}}}\right)^4\right] + \frac{\sigma_{\mathrm{nf}}B_0^2}{T_{\infty}}(u_{\mathrm{b}}^2 + v_{\mathrm{b}}^2)^2. \tag{26}$$

The characteristics of entropy generation can be expressed as

$$\mathrm{EG}_0 = \frac{k_{\mathrm{f}}(T_{\mathrm{wb}} - T_{\infty})^2}{x_{\mathrm{b}}^2T_{\infty}^2}. \tag{27}$$

Similarity transformation (10) can be used to write the dimensionless form of the entropy generation as

$$\mathrm{NG}^{*} = \frac{\mathrm{EG}}{\mathrm{EG}_0} = \frac{k_{\mathrm{nf}}}{k_{\mathrm{f}}}\left(\frac{m+1}{2}\right)\mathrm{Re}_{x_{\mathrm{b}}x_{\mathrm{b}}}S'^2 + \left(\frac{\mu_{\mathrm{nf}}}{\mu_{\mathrm{f}}} + \Sigma_{\mathrm{a}}\right)\left(\frac{m+1}{2}\right)\frac{\mathrm{Br}_{\mathrm{b}}\mathrm{Re}_{x_{\mathrm{b}}x_{\mathrm{b}}}}{\Omega_{\mathrm{b}}}(F'' + E_{\mathrm{c}}G'')^2 - \frac{\Sigma_{\mathrm{a}}\Sigma_{\mathrm{b}}}{2}\left(\frac{m+1}{2}\right)^2\frac{\mathrm{Br}_{\mathrm{b}}\mathrm{Re}_{x_{\mathrm{b}}x_{\mathrm{b}}}}{\Omega_{\mathrm{b}}}(F'' + E_{\mathrm{c}}G'')^4 + \frac{\sigma_{\mathrm{nf}}}{\sigma_{\mathrm{f}}}M_{\mathrm{c}}\frac{\mathrm{Br}_{\mathrm{b}}\mathrm{Re}_{x_{\mathrm{b}}x_{\mathrm{b}}}}{\Omega_{\mathrm{b}}}(F'^2 + E_{\mathrm{c}}^2G'^2), \tag{28}$$

where $E_c = \frac{B}{A}$, $\mathrm{B\eth}_b = \frac{\mu_f u_{wb}^2}{k_f(T_{wb} - T_\infty)}$, $\Omega_b = \frac{(T_{wb} - T_\infty)}{T_\infty}$ stand for stretching rate ratio parameter, Brinkman number, and temperature difference parameter, respectively.

4 Temporal stability analysis

We have examined the stability of dual (upper and lower) solutions as time progresses. Initially, Merkin [42] introduced the procedure of the stability analysis, and later on, Weidman *et al.* [43] followed. First, we begin with the newly established variables for the assessed process as follows:

$$\begin{aligned} &u_b = Ax_b^m \frac{\partial F(\xi, \tau_b)}{\partial \xi},\ v_b = Bx_b^m \frac{\partial G(\xi, \tau_b)}{\partial \xi}, \\ &\xi = (A/\upsilon_f)^{1/2} C(x_b) z_b,\ S(\xi, \tau_b) = \frac{T_b - T_\infty}{T_{wb} - T_\infty} \\ &w_b = -\frac{\sqrt{A\upsilon_f}}{C}\left[m x_b^{m-1} F(\xi, \tau_b) + x_b^m \frac{C_{x_b}}{C}\left\{ \xi \frac{\partial F(\xi, \tau_b)}{\partial \xi} \right.\right. \\ &\qquad \left.\left. - F(\xi, \tau_b) \right\}\right], \end{aligned} \tag{29}$$

where $\tau_b = Ax_b^{m-1} t_a$ signifies the new-fangled non-dimensional time. In addition, the following can occur in the state by applying the aforementioned Eq. (29) to the time-dependent or unstable form of the necessary leading Eqs. (6)–(8) as well as Eqs. (13), (14), and (17). Thus,

$$\begin{aligned} &\frac{1}{\rho_{nf}/\rho_f}\left(\frac{\mu_{nf}}{\mu_f} + \Sigma_a\right)\frac{\partial^3 F}{\partial \xi^3} - \left(\frac{m+1}{4}\right)\frac{\Sigma_a \Sigma_b}{\rho_{nf}/\rho_f}\left(\frac{\partial^2 F}{\partial \xi^2}\right)^2 \frac{\partial^3 F}{\partial \xi^3} \\ &\quad + F\frac{\partial^2 F}{\partial \xi^2} - \frac{2m}{m+1}\left(\frac{\partial F}{\partial \xi}\right)^2 \\ &\quad - \left(\frac{2}{m+1}\right)\frac{\sigma_{nf}/\sigma_f}{\rho_{nf}/\rho_f} M_c \frac{\partial F}{\partial \xi} - \left(\frac{2}{m+1}\right)\frac{\partial^2 F}{\partial \xi \partial \tau_b} = 0, \end{aligned} \tag{30}$$

$$\begin{aligned} &\frac{1}{\rho_{nf}/\rho_f}\left(\frac{\mu_{nf}}{\mu_f} + \Sigma_a\right)\frac{\partial^3 G}{\partial \xi^3} - \left(\frac{m+1}{4}\right)\frac{\Sigma_a \Sigma_b}{\rho_{nf}/\rho_f} E_c^2 \left(\frac{\partial^2 G}{\partial \xi^2}\right)^2 \frac{\partial^3 G}{\partial \xi^3} \\ &\quad + F\frac{\partial^2 G}{\partial \xi^2} - \frac{2m}{m+1}\left(\frac{\partial F}{\partial \xi}\right)\left(\frac{\partial G}{\partial \xi}\right) \\ &\quad - \left(\frac{2}{m+1}\right)\frac{\sigma_{nf}/\sigma_f}{\rho_{nf}/\rho_f} M_c \frac{\partial G}{\partial \xi} - \left(\frac{2}{m+1}\right)\frac{\partial^2 G}{\partial \xi \partial \tau_b} = 0, \end{aligned} \tag{31}$$

$$\begin{aligned} &\frac{k_{nf}/k_f}{\mathrm{Pr}(\rho c_p)_{nf}/(\rho c_p)_f}\frac{\partial^2 S}{\partial \xi^2} + F\frac{\partial S}{\partial \xi} \\ &\quad + \left(\frac{2}{m+1}\right)\frac{\left(\frac{\rho_{nf}}{\rho_f}\right)\left(\frac{k_{nf}}{k_f}\right)}{\mathrm{Pr}\frac{(\rho c_p)_{nf}}{(\rho c_p)_f}\left(\frac{\mu_{nf}}{\mu_f}\right)}[A_c^* e^{-\xi} + B_c^* S] - \left(\frac{2}{m+1}\right)\frac{\partial S}{\partial \tau_b}, \end{aligned} \tag{32}$$

according to the relevant BCs:

$$\begin{cases} G(0, \tau_b) = 0,\ F(0, \tau_b) = f_{wc},\ \dfrac{\partial F(0, \tau_b)}{\partial \xi} = \dfrac{\partial G(0, \tau_b)}{\partial \xi^2} \\ \qquad = \gamma_c,\ S(0, \tau_b) = 1, \\ \dfrac{\partial G(\xi, \tau_b)}{\partial \xi} \to 0,\ \dfrac{\partial F(\xi, \tau_b)}{\partial \xi} \to 0,\ S(\xi, \tau_b) \to 0 \\ \text{as } \xi \to \infty. \end{cases} \tag{33}$$

Following that the subsequent relationships are regarded as follows (see Weidman *et al.* [43]):

$$\begin{aligned} F(\xi, \tau_b) &= F_0(\xi) + e^{-\Gamma_b \tau_b} f(\xi), \\ G(\xi, \tau_b) &= G_0(\xi) + e^{-\Gamma_b \tau_b} g(\xi), \\ S(\xi, \tau_b) &= S_0(\xi) + e^{-\Gamma_b \tau_b} s(\xi), \end{aligned} \tag{34}$$

where the stable solution of $F = F_0$, $G = G_0$, and $S = S_0$ can effortlessly perturb PDEs (6)–(8). Furthermore, the functions $f(\xi)$, $g(\xi)$, and $s(\xi)$ in Eq. (34) are moderately minor as associated with $F_0(\xi)$, $G_0(\xi)$, and $S_0(\xi)$. The stability of the results is concluded by the sign (positive or negative) of the eigenvalue Γ_b. Through setting, $\tau_b = 0$, we have $f(\xi) = f_0(\xi)$, $g(\xi) = g_0(\xi)$, and $s(\xi) = s_0(\xi)$. Using Eq. (34) in Eqs. (30)–(32) yields the linearized eigenvalue problem

$$\begin{aligned} &\frac{1}{\rho_{nf}/\rho_f}\left(\frac{\mu_{nf}}{\mu_f} + \Sigma_a\right) f_0''' - \left(\frac{m+1}{4}\right)\frac{\Sigma_a \Sigma_b}{\rho_{nf}/\rho_f}(2F_0'' F_0''' f_0'' \\ &\quad + F_0'' 2f_0''') + F_0 f_0'' + f_0 F_0'' \\ &\quad - \frac{4m}{m+1} F_0' f_0' - \left(\frac{2}{m+1}\right)\frac{\sigma_{nf}/\sigma_f}{\rho_{nf}/\rho_f} M_c f_0' + \left(\frac{2}{m+1}\right)\Gamma_b f_0' \\ &\quad = 0, \end{aligned} \tag{35}$$

$$\begin{aligned} &\frac{1}{\rho_{nf}/\rho_f}\left(\frac{\mu_{nf}}{\mu_f} + \Sigma_a\right) g_0''' - \left(\frac{m+1}{4}\right)\frac{\Sigma_a \Sigma_b}{\rho_{nf}/\rho_f} E_c^2 (2G_0'' G_0''' g_0'' \\ &\quad + G_0'' 2g_0''') + F_0 g_0'' + f_0 G_0'' \\ &\quad - \frac{2m}{m+1}(F_0' g_0' + f_0' G_0') - \left(\frac{2}{m+1}\right)\frac{\sigma_{nf}/\sigma_f}{\rho_{nf}/\rho_f} M_c g_0' \\ &\quad + \left(\frac{2}{m+1}\right)\Gamma_b g_0' = 0, \end{aligned} \tag{36}$$

$$\begin{aligned} &\frac{k_{nf}/k_f}{\mathrm{Pr}(\rho c_p)_{nf}/(\rho c_p)_f} s_0'' + F_0 s_0' + f_0 S_0' \\ &\quad + \left(\frac{2}{m+1}\right)\frac{\left(\frac{\rho_{nf}}{\rho_f}\right)\left(\frac{k_{nf}}{k_f}\right)}{\mathrm{Pr}\frac{(\rho c_p)_{nf}}{(\rho c_p)_f}\left(\frac{\mu_{nf}}{\mu_f}\right)} B_c^* s_0 + \left(\frac{2}{m+1}\right)\Gamma_b s_0, \end{aligned} \tag{37}$$

subject to BCs

$$\begin{cases} g_0(0) = 0,\ f_0(0) = 0,\ f_0'(0) = g_0'(0) = 0,\ s_0(0) = 0, \\ g_0'(\xi) \to 0,\ f_0'(\xi) \to 0,\ s_0(\xi) \to 0 \text{ as } \xi \to \infty. \end{cases} \tag{38}$$

Adjusting the value of $f_0''(0)$, $g_0''(0)$ or $s_0'(0)$ yields the equivalent positive or negative values of Γ_b in the aforementioned Eqs. (35), (36), and (37). Maintaining generality without losing, we set $f_0''(0) = 1$ and discover the eigenvalues Γ_b by solving the set of related Eqs. (35)–(38) (see Khan *et al.* [44] and Duguma *et al.* [45]).

5 Numerical method

The dimensionless group of extremely difficult nonlinear Eqs. (18), (19), and (21) along with BCs (23) cannot be solved analytically or exactly. Consequently, the collocation formula has been used to numerically solve these dimensionless form equations through the fourth-order boundary value problem (bvp4c). This code, which is included in MATLAB, provides the solution for the well-known 3-stage Lobatto IIIA formula, which is likewise based on the finite difference method. The new variables must first be introduced for the bvp4c package to function. Then, we can use them to obtain the set of first-order equations from the governing dimensionless equations. Several reasonable initial guesses were needed for the software to get an improved result. Furthermore, the BCs when ξ approaches to infinity are replaced by those at $\xi = \xi_\infty$. Asymptotically convergence criteria and precision up to 10^{-6} level error tolerance are met in every instance during the iteration process. More about this procedure can be seen in the article Shampine *et al.* [46].

6 Analysis of the results

This section of the study shows the full physical clarifications of our entire results for all of the different contained embedded parameters. Table 3 displays a comparison of the HTR for the different values of Pr based on the accessible works when $\varphi_{s_c} = f_{wc} = \Sigma_a = \Sigma_b = M_c = A_c^* = B_c^* = 0$, $m = 1.0$, and $\gamma_c = 1.0$. The available and prior findings are nicely aligned and produce an excellent sound based on the results of the above table. The smallest numerical eigenvalues Γ_b for a diverse value of γ_c are displayed in Table 4. According to this table, the upper branch (UB) solution is physically and temporally feasible since the value of the least eigenvalue is positive. It is evident from the negative value of γ_c that the lower branch (LB) solution is unstable and not consistent with physical reality. This perfect match can reassure us that the current executed scheme is well enough to apply and locate the unobtainable results. Figures 2–15 are prepared to examine the influence of the sundry physical constraints on the shear stress in the SMW, SNW, and HTR. Also, the entropy profiles are portrayed in Figures 16–18. In addition, the smallest eigenvalues Γ_b are also shown by the graph (Figure 19). The considered model proposes two solutions, an UB solution and an LB solution for the variance of the sundry parameters. The UB solution is denoted by solid blue lines, and the LB solution is denoted by dashed blue lines. On the other hand, the intersection of the UB and LB is commonly referred to as a bifurcation point.

Figures 2–4 illustrate the influence of m on the shear stress coefficient in the SMW direction, shear stress coefficient in the SNW direction, and HTR of the $NAC_6H_7O_6$-based $CoFe_2O_4$ nanoparticles, respectively. The UB and LB outcomes are created in these graphs for the circumstance of the suction parameter. The products of friction factor in both directions of the UBS for $NAC_6H_7O_6$-based $CoFe_2O_4$ nanoparticles improve with the remarkable augmentation of m *versus* mass suction parameter f_{wc}. However, opposite monotonic behaviors are established for the LBS with

Table 3: Numerical comparison of HT values for the selected sundry choices of Pr when $f_{wc} = \Sigma_a = \Sigma_b = M_c = A_c^* = B_c^* = \varphi_{s_c} = 0$, $\gamma_c = 1.0$, and $m = 1.0$

Pr	Devi and Devi [47]	Wang [48]	Khan and Pop [49]	Present results
2.0	0.91135	0.9114	0.9113	0.9113543
6.13	1.75968	—	—	1.7596836
7.0	1.89540	1.8954	1.8954	1.8954001
20.0	3.35390	3.3539	3.3539	3.3539025

Table 4: Smallest eigenvalues Γ_b for a diverse value of γ_c when $\Sigma_a = 0.1$, $m = 2.0$, $\varphi_{s_c} = 0.025$, $E_c = 0.5$, $A_c^* = B_c^* = 0.1$, $\Sigma_b = 0.5$, and $f_{wc} = 2.0$

γ_c	Smallest eigenvalues γ_c	
	Upper solution	Lower solution
−0.3	1.9435	−1.6435
−0.5	1.8317	−1.5345
−0.8	1.6673	−1.3672
−1.0	1.3534	−1.1427
−1.05	1.2234	−1.0584
−1.1	1.0234	−0.9145
−1.12	0.9367	−0.8246
−1.14	0.8466	−0.7657
−1.16	0.7534	−0.6567
−1.18	0.6393	−0.5389
−1.2	0.4534	−0.4358
−1.21	0.3638	−0.2167
−1.214	0.0145	−0.0250

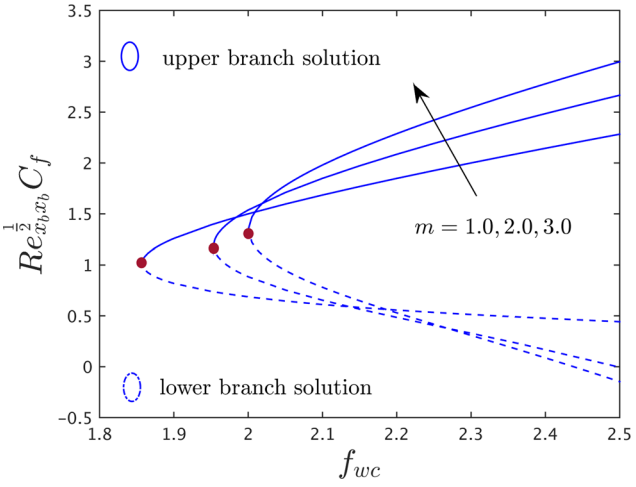

Figure 2: Shear stress in the SMW direction *versus* f_{wc} for distinct values of m when $\Sigma_a = 0.1$, $\Sigma_b = 0.5$, $M_c = 0.1$, $E_c = 0.5$, $A_c^* = B_c^* = 0.1$, $\varphi_{sc} = 0.025$, and $\gamma_c = -1.0$.

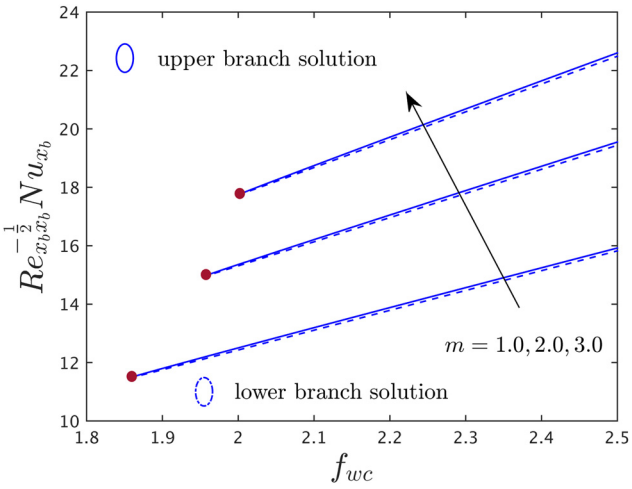

Figure 4: Variation of HTR *versus* f_{wc} for distinct values of m when $\Sigma_a = 0.1$, $\Sigma_b = 0.5$, $M_c = 0.1$, $E_c = 0.5$, $A_c^* = B_c^* = 0.1$, $\varphi_{sc} = 0.025$, and $\gamma_c = -1.0$.

superior consequences of m. Besides, the condition is noted that m is the power exponent constraint for the momentum distribution, whereas $m = 1$ and $m > 1$ refer to the instance of linear and nonlinear (power-law) stretching/shrinking velocity, respectively. As proved in Figure 4, the higher power-law index parameter value upsurges the HTR in both (UB and LB) outcomes. Additionally, the rate of HT is higher for the power-law index parameter values $m = 2, 3$ as compared to the linear case $m = 1$. Also, the solid gray ball in all three above-stated graphs denotes the point of bifurcation where the UB and LB solutions are merged. At this particular point, the outcomes of the problem are unique and mathematically it is denoted by $f_{wc} = f_{wc}C$, where $f_{wc}C$ is the bifurcation or critical point. This bifurcation point will be changed *via* changing the values of m, see the located graphs. Meanwhile, the outcomes are not unique for the case of $f_{wc} > f_{wc}C$, and no solutions exist for the case of $f_{wc} < f_{wc}C$ when we do the variations in the power-law index parameter $f_{wc} = f_{wc}C$. With higher values of m, the absolute or magnitude of the bifurcation values are augmented. This design highlights that the BL separation decline from the HPS with greater impacts of m.

The effect of Σ_b on the friction factor coefficients in the directions of SMW and SNW of the $NAC_6H_7O_6$-based $CoFe_2O_4$ nanoparticles for the UBS and LBS are presented

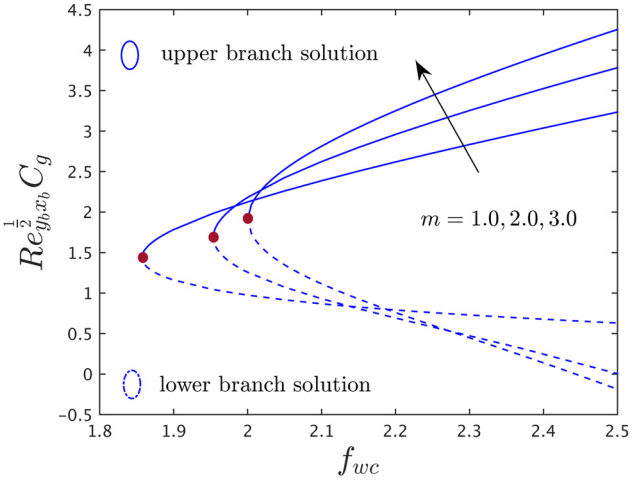

Figure 3: Shear stress in the SNW direction *versus* f_{wc} for distinct values of m when $\Sigma_a = 0.1$, $\Sigma_b = 0.5$, $M_c = 0.1$, $E_c = 0.5$, $A_c^* = B_c^* = 0.1$, $\varphi_{sc} = 0.025$, and $\gamma_c = -1.0$.

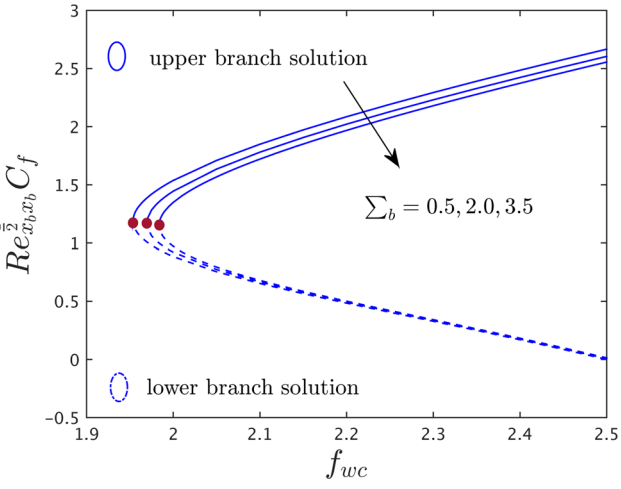

Figure 5: Shear stress in the SMW direction *versus* f_{wc} for distinct values of Σ_b when $\Sigma_a = 0.1$, $m = 2.0$, $M_c = 0.1$, $E_c = 0.5$, $A_c^* = B_c^* = 0.1$, $\varphi_{sc} = 0.025$, and $\gamma_c = -1.0$.

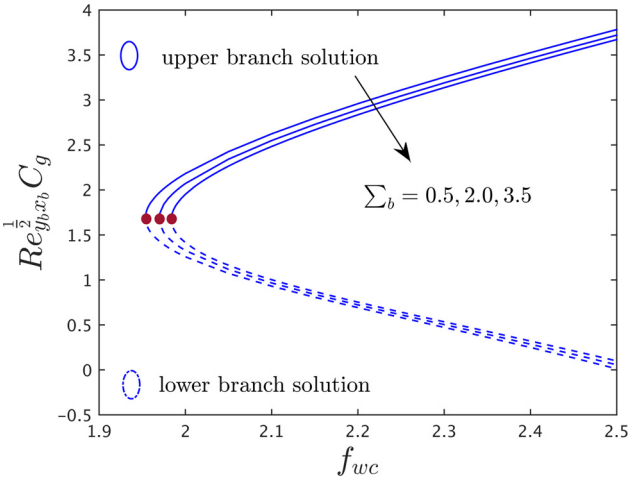

Figure 6: Shear stress in the SNW direction *versus* f_{wc} for distinct values of Σ_b when $\Sigma_a = 0.1$, $m = 2.0$, $M_c = 0.1$, $E_c = 0.5$, $A_c^* = B_c^* = 0.1$, $\varphi_{sc} = 0.025$, and $\gamma_c = -1.0$.

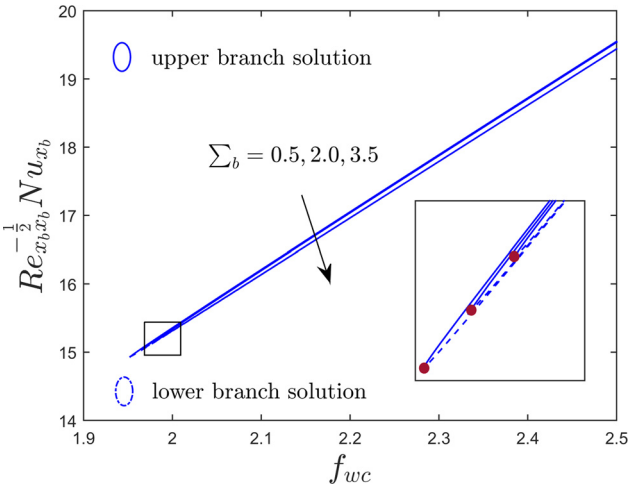

Figure 7: Variation of HTR *versus* f_{wc} for distinct values of Σ_b when $\Sigma_a = 0.1$, $m = 2.0$, $M_c = 0.1$, $E_c = 0.5$, $A_c^* = B_c^* = 0.1$, $\varphi_{sc} = 0.025$, and $\gamma_c = -1.0$.

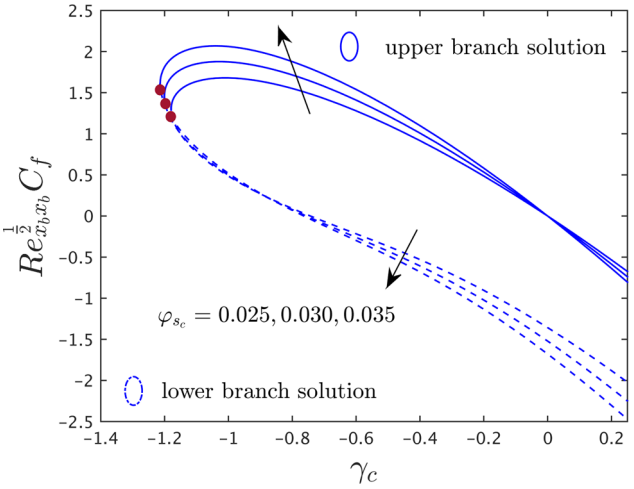

Figure 8: Shear stress in the SMW direction *versus* γ_c for distinct values of φ_{sc} when $\Sigma_a = 0.1$, $m = 2.0$, $M_c = 0.1$, $E_c = 0.5$, $A_c^* = B_c^* = 0.1$, $\Sigma_b = 0.5$, and $f_{wc} = 2.0$.

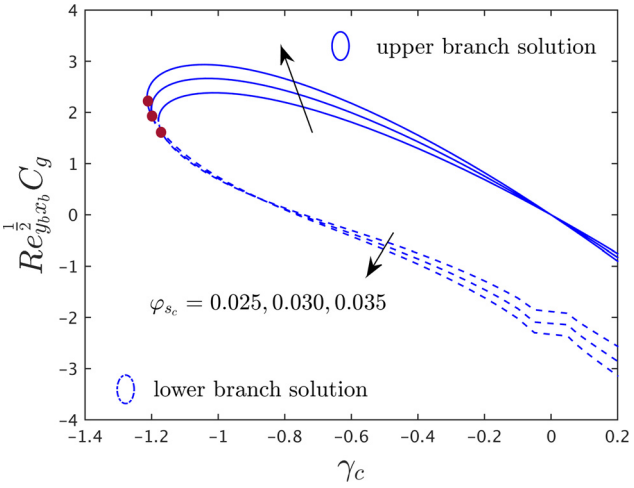

Figure 9: Shear stress in the SNW direction *versus* γ_c for distinct values of φ_{sc} when $\Sigma_a = 0.1$, $m = 2.0$, $M_c = 0.1$, $E_c = 0.5$, $A_c^* = B_c^* = 0.1$, $\Sigma_b = 0.5$, and $f_{wc} = 2.0$.

in Figures 5 and 6. From these graphical structures, it is recognized that the friction factor coefficients in both directions decline for the UBS with growing the material or non-Newtonian (EPF) parameter Σ_b but a notable augmentation is observed in the LBS. On the other hand, the HTR with rising values of Σ_b for the outcomes of UB as well as LB is shown in Figure 7. Superior Σ_b central to a considerable improvement in the values of HTR for the LBS, whereas retardation is noticed for the branch of the US. Generally, the absolute viscosity μ_f and the material parameter Σ_b follow the inverse relation. Therefore, a significant increase in the value of Σ_b produces a reduction in the value of μ_f, and as a consequence, the velocity profile is boosted. Thus, the friction factor coefficients in both routes of the $NAC_6H_7O_6$-based $CoFe_2O_4$ nanoparticles should, therefore, decrease as the velocity increases. In addition, the bifurcation value developments in magnitude or absolute due to stronger impacts of the material parameter Σ_b. Thus, a delay in the separation of the BLF from the HPS is perceived because of the higher consequence in the values of Σ_b.

Figures 8 and 9 illustrate the outcome of the friction factor coefficients in both directions of the regular $NAC_6H_7O_6$-based $CoFe_2O_4$ nanoparticles for the UBS and LBS with growing values of φ_{s_c}. The outcome in both graphs shows that the shear stress for the UBS declines in the

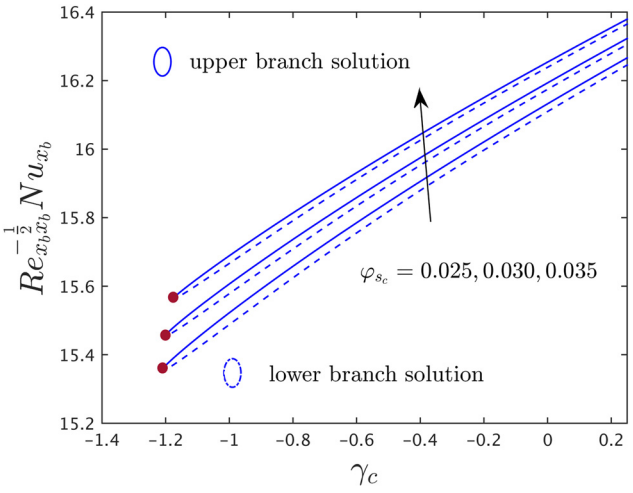

Figure 10: Variation of HTR *versus* γ_c for distinct values of φ_{s_c} when $\Sigma_a = 0.1$, $m = 2.0$, $M_c = 0.1$, $E_c = 0.5$, $A_c^* = B_c^* = 0.1$, $\Sigma_b = 0.5$, and $f_{wc} = 2.0$.

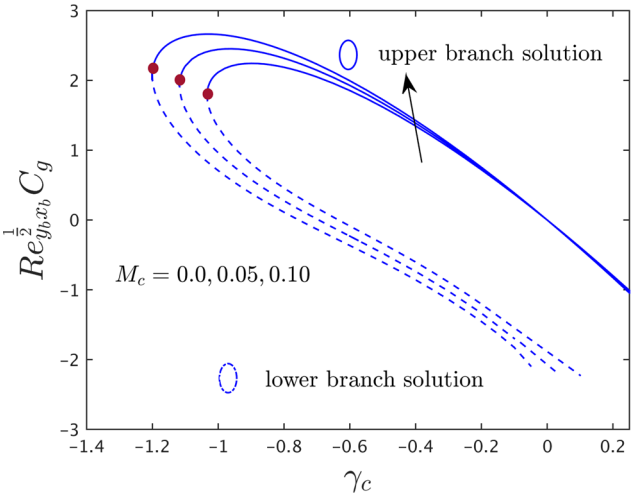

Figure 12: Shear stress in the SNW direction *versus* γ_c for distinct values of M_c when $\Sigma_a = 0.1$, $m = 2.0$, $\varphi_{s_c} = 0.025$, $E_c = 0.5$, $A_c^* = B_c^* = 0.1$, $\Sigma_b = 0.5$, and $f_{wc} = 2.0$.

situation of stretching and escalates in the situation of shrinking due to the superior effects of φ_{s_c}. However, continuous reductions are seen for the LBS in the case of deformable with increasing φ_{s_c}. Figure 10 exhibits the influences of φ_{s_c} on the HTR of the $NAC_6H_7O_6$-based $CoFe_2O_4$ nanoparticles for the UB and LB solutions. It is professed that the outcome of HTR escalates owing to the advanced values of φ_{s_c}. Generally, the EPF flow TCN develops with higher impacts of φ_{s_c}, as a fallout, the HT upsurges. Additionally, two separate (UB and LB) branches meet at a single location known as a critical point. At this position, the results are exceptional (or unique) and scientifically it is expressed as $\gamma_c = \gamma_c C$, where $\gamma_c C$ corresponds the critical point. For the specific domain areas such as $\gamma_c C < \gamma_c < \infty$, and $-\infty < \gamma_c < \gamma_c C$, the dual outcomes and no outcomes exist, respectively (see Elatter *et al.* [50]). Owing to greater impacts of φ_{s_c}, the bifurcation or critical values in magnitude declines. This behavior is triggered due to the stronger effects of φ_{s_c}, and hence the rise of the flow separation from the HPS.

The consequence of the magnetic parameter M_c on the friction factor coefficients in both directions and HTR of the $NAC_6H_7O_6$-based $CoFe_2O_4$ nanoparticles for the UB and LB solutions are revealed in Figures 11–13, respectively. For

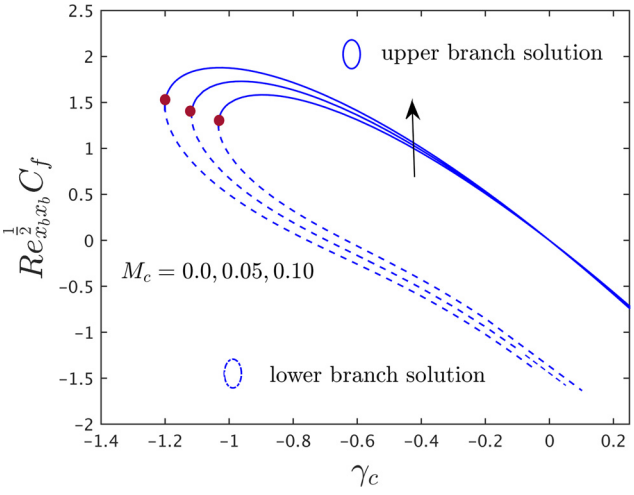

Figure 11: Shear stress in the SMW direction *versus* γ_c for distinct values of M_c when $\Sigma_a = 0.1$, $m = 2.0$, $\varphi_{s_c} = 0.025$, $E_c = 0.5$, $A_c^* = B_c^* = 0.1$, $\Sigma_b = 0.5$, and $f_{wc} = 2.0$.

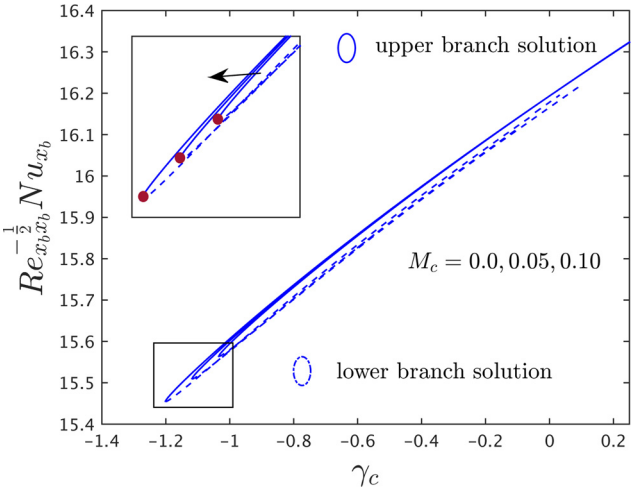

Figure 13: Variation of HTR *versus* γ_c for distinct values of M_c when $\Sigma_a = 0.1$, $m = 2.0$, $\varphi_{s_c} = 0.025$, $E_c = 0.5$, $A_c^* = B_c^* = 0.1$, $\Sigma_b = 0.5$, and $f_{wc} = 2.0$.

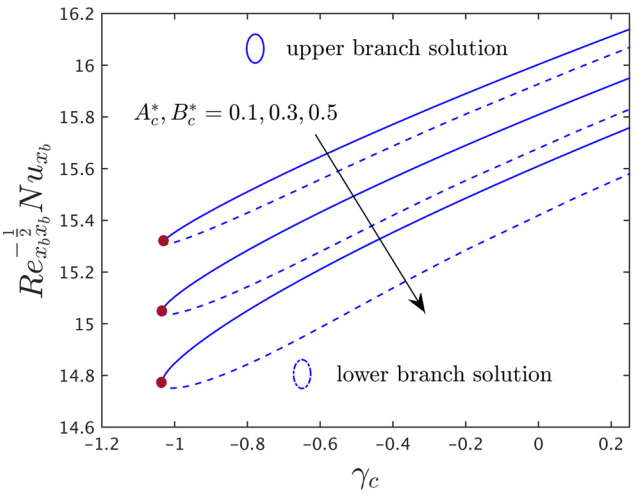

Figure 14: Variation of HTR *versus* γ_c for distinct values of $A_c^*, B_c^* > 0$ when $\Sigma_a = 0.1m = 2.0$, $\varphi_{sc} = 0.025$, $E_c = 0.5$, $M_c = 0.1$, $\Sigma_b = 0.5$, and $f_{wc} = 2.0$.

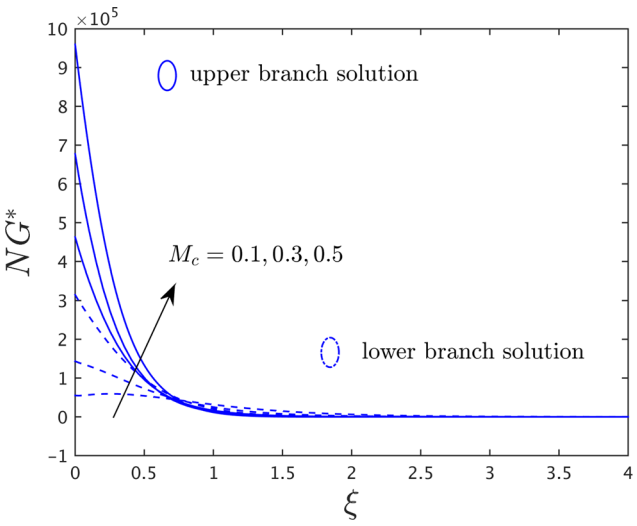

Figure 16: Variation of entropy for distinct values of M_c when $\Sigma_a = 0.1$, $m = 2.0$, $\varphi_{sc} = 0.025$, $E_c = 0.5$, $A_c^* = B_c^* = 0.1$, $\Sigma_b = 0.5$, $Br_b = 1.0$, $\Omega_b = 0.01$, $Re_{x_b x_b} = 10$, and $f_{wc} = 2.0$.

rising M_c, the values of friction factor coefficients in both paths upsurge for the UBS, while the trends are reversed for the LBS. More especially, the outcomes for the UBS exist if we go forward from shrinking to stretching plane surface, but for the case of stretching, the LBS diminished due to higher value of M_c. However, the HTR is also enriching for the UB and as well as for the LB results owing to the superior impacts of M_c. Physically, the Lorentz force operates along the fluid flow due to the implementation of an MF in the laminar flow condition. The Lorentz force generates internal resistance within the boundary layer, resulting in a dragging force. Therefore, the fluid particles undergo a reduction in momentum due to the consequence of the Lorentz force, as a result, the velocity profiles decline. Also, the friction force and the velocity follow the basic law of physics called a direct relation. According to this relation, the friction factor coefficients intensify in both routes. Besides, the magnitude of the bifurcation values uplifts with higher magnetic parameter and hence delays the BL flow separation from the HPS.

Figures 14 and 15 portray the impact of the internal heat source parameter, $A_c^*, B_c^* > 0$, and heat sink constraint, $A_c^*, B_c^* < 0$, on the HTR of the $NAC_6H_7O_6$)-based

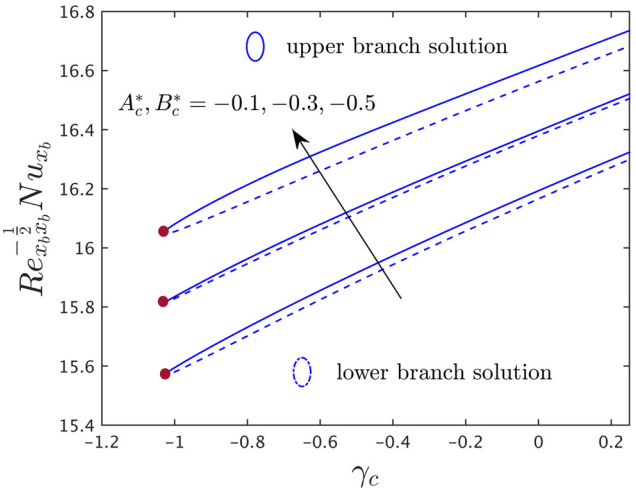

Figure 15: Variation of HTR *versus* γ_c for distinct values of $A_c^*, B_c^* < 0$ when $\Sigma_a = 0.1$ $m = 2.0$, $\varphi_{sc} = 0.025$, $E_c = 0.5$, $M_c = 0.1$, $\Sigma_b = 0.5$, and $f_{wc} = 2.0$.

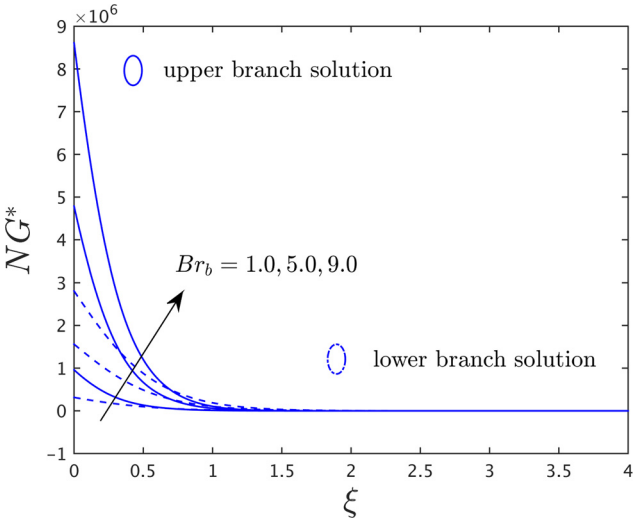

Figure 17: Variation of entropy for distinct values of Br_b when $\Sigma_a = 0.1$, $m = 2.0$, $\varphi_{sc} = 0.025$, $E_c = 0.5$, $A_c^* = B_c^* = 0.1$, $\Sigma_b = 0.5$, $M_c = 0.1$, $\Omega_b = 0.01$, $Re_{x_b x_b} = 10$, and $f_{wc} = 2.0$.

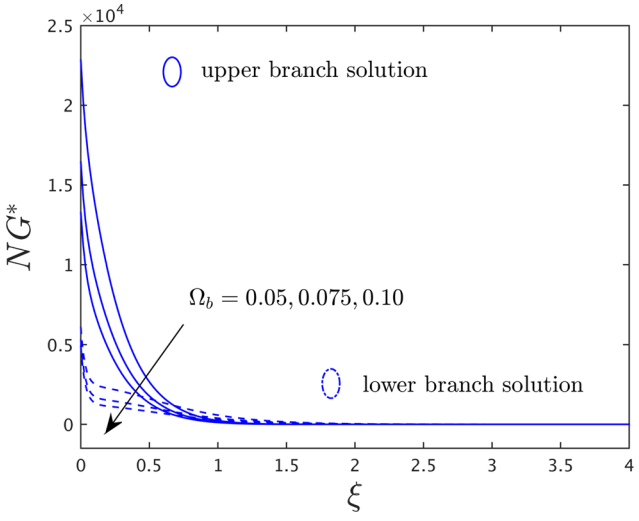

Figure 18: Variation of entropy for distinct values of Ω_b when Σ_a = 0.1, m = 2.0, φ_{s_c} = 0.025, E_c = 0.5, A_c^* = B_c^* = 0.1, Σ_b = 0.5, Br_b = 1.0, M_c = 0.1, $Re_{x_b x_b}$ = 10, and f_{wc} = 2.0.

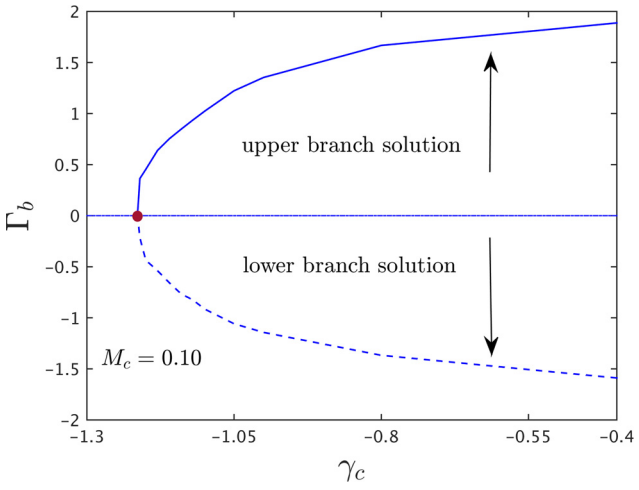

Figure 19: Variation of smallest eigenvalues Γ_b for a diverse value of γ_c.

$CoFe_2O_4$ nanoparticles for the dual branches, respectively. The greater impact of $A_c^*, B_c^* > 0$ leads to a substantial decline in the UB as well as the LB outcomes. However, a very opposite pattern or tendency is realized in Figure 15 when we increase the values of $A_c^*, B_c^* < 0$. Owing to alteration the simultaneous positive and negative values of A_c^* and B_c^*, as a result, the critical values are the same (Figures 14 and 15). In light of this, the difference between the UB and LB solution curves is preferable for the situation of a heat source as opposed to the effect of a heat sink parameter.

Figures 16–18 show the behavior of the entropy generation for both solution branches due to the different values of M_c, Br_b, and Ω_b. These profiles suggest that the entropy accelerates by either improving magnetic or Brinkman numbers. Meanwhile, it is decelerated due to the higher impact of the temperature difference parameter Ω_b. Physically, entropy is generated by all irreversibility mechanisms, and as a result, the Lorentz forces cause entropy to increase. Increasing the Brinkman number leads to greater amounts of entropy generation created by the irreversibility of the fluid friction.

Figure 19 shows the smallest eigenvalues Γ_b against the shrinking/stretching parameter γ_c for the particular selected magnetic parameter value such as M_c = 0.10 when Σ_a = 0.1, m = 2.0, φ_{s_c} = 0.025, E_c = 0.5, A_c^* = B_c^* = 0.1, Σ_b = 0.5, and f_{wc} = 2.0. From the graph, it is seen that for positive values of Γ_b the term $e^{-\Gamma_b \eta_b} \to 0$ as $\Gamma_b \to \infty$ and it explodes for higher negative values. In other words, the sign of the smallest eigenvalue Γ_b for the first solution is positive, which signifies the stability characteristics of the solutions. Meanwhile, the values of smallest eigenvalue Γ_b for the second solution are negative, which indicates the second solution long-term instability. As a result, the upper solution is physically more trustworthy than the lower solution since its stability reflects its physical reliability.

7 Final remarks

This article aims to investigate the $NAC_6H_7O_6$-based $CoFe_2O_4$ nanoparticles on magneto flow and HT toward a nonlinear DHPS with irregular heat source/sink and power-law velocity. The dual or binary (UB and LB) solutions were obtained using the bvp4c solver. The reliability and validity of results were tested through stability analysis in a few instances where it was determined that the current results were equivalent to the prior ones. Numerous portraits have been plotted to examine the effects of the various relevant constraints on the shear stress in the respective SMW and SNW directions, rate of HT and entropy generation profiles. We can draw the following important conclusions from this investigation as follows:

- Multiple solutions are provoked only if the strength of suction is applied and in the region of the shrinking sheet.
- The shear stress in both directions as well as the HTR augment due to the power-law index m and the suction parameter.
- The shear stress in both directions and HTR decline due to the EPF parameter.
- The sodium alginate-based $CoFe_2O_4$ nanoparticles boost the HTR in both resolutions while augmenting the shear stress in SMW and SNW directions in the UB solution and decline in the LB solution.

- The presence of a magnetic parameter ultimately augments the shear stress in the UB solution and declines in the LB solution, whereas the HTR uplifts in both solutions.
- The HTR declines in the presence of source parameter and uplift due to sink parameter in both UB and LB solutions.
- The entropy generation accelerates due to magnetic and Brinkman numbers, while the opposite trend is observed due to the temperature difference parameter.
- From the temporal stability analysis, it is recognized that the UB solutions are stable and physically acceptable.

Acknowledgments: This work was funded by the Deanship of Scientific Research at Princess Nourah bint Abdulrahman University, through the Research Groups Program Grant no. (RGP-1444-0060).

Funding information: This work was funded by the Deanship of Scientific Research at Princess Nourah bint Abdulrahman University, through the Research Groups Program Grant no. (RGP-1444-0060).

Author contributions: Conceptualization, S.E., and U.K.; methodology, S.E., A.I., and U.K.; software, A.I., A.Z., S.E., and U.K.; validation, N.A., A.M.A., U.K., A.Z., and A.I.; formal analysis, A.I., A.M.A., N.A., and A.Z.; investigation, A.I., and A.Z.; resources, A.I.; data curation, A.I., A.Z., U.K., and S.E., writing – original draft preparation, N.A., U.K., and A.M.A.; writing – review and editing, N.A., A.Z., and A.M.A.; visualization, A.Z.; supervision, A.I.; project administration, N.A., A.M.A. and S.E.; funding acquisition, N.A., A.M.A. and S.E. All authors have accepted responsibility for the entire content of this manuscript and approved its submission.

Conflict of interest: The authors state no conflict of interest.

Data availability statement: The datasets generated and/or analyzed during the current study are available from the corresponding author on reasonable request.

References

[1] Nima NI, Salawu SO, Ferdows M, Shamshuddin MD, Alsenafi A, Nakayama A. Melting effect on non-Newtonian fluid flow in gyrotactic microorganism saturated non-Darcy porous media with variable fluid properties. Appl Nanosci. 2020;10:3911–24.

[2] Gorder RAV, Sweet E, Vajravelu K. Nano boundary layers over stretching surfaces. Commun Nonlinear Sci Numer Simul. 2010;15(6):1494–500.

[3] Das K. Slip flow and convective heat transfer of nanofluids over a permeable stretching surface. Comput Fluids. 2012;64:34–42.

[4] Noghrehabadi A, Ghalambaz M, Izadpanahi E, Pourrajab R. Effect of magnetic field on the boundary layer flow, heat, and mass transfer of nanofluids over a stretching cylinder. J Heat Mass Transf Res. 2014;1(1):9–16.

[5] Freidoonimehr N, Rashidi MM, Mahmud S. Unsteady MHD free convective flow past a permeable stretching vertical surface in a nano-fluid. Int J Therm Sci. 2015;87:136–45.

[6] Naramgari S, Sulochana C. Dual solutions of radiative MHD nanofluid flow over an exponentially stretching sheet with heat generation/absorption. Appl Nanosci. 2016;6(1):131–9.

[7] Makinde OD, Mabood F, Ibrahim SM. Chemically reacting on MHD boundary layer flow of nanofluids over a nonlinear stretching sheet with heat source/sink and thermal radiation. Therm Sci. 2018;22:495–506.

[8] Acharya N, Bag R, Kundu PK. Influence of Hall current on radiative nanofluid flow over a spinning disk: A hybrid approach. Phys E: Low-dimens Syst Nanostruct. 2019;111:103–12.

[9] Zaib A, Haq RU, Sheikholeslami M, Khan U. Numerical analysis of effective Prandtl model on mixed convection flow of γAl_2O_3–H_2O nanoliquids with micropolar liquid driven through wedge. Phys Scr. 2020;95:035005.

[10] Khan U, Zaib A, Madhukesh JK, Elattar S, Eldin SM, Ishak A, et al. Features of radiative mixed convective heat transfer on the slip flow of nanofluid past a stretching bended sheet with activation energy and binary reaction. Energies. 2022;15:7613.

[11] Divya S, Eswaramoorthi S, Loganathan K. Numerical computation of Ag/Al_2O_3 nanofluid over a Riga Plate with heat sink/source and non-Fourier heat flux model. Math Comput Appl. 2023;28(1):20.

[12] Genc S, Derin B. Synthesis and rheology of ferrofluids: A review. Curr Opin Chem Eng. 2014;3:118–24.

[13] Issa B, Obaidat IM, Albiss BA, Haik Y. Magnetic nanoparticles: Surface effects and properties related to biomedicine applications. Int J Mol Sci. 2013;14(11):21266–305.

[14] Khan ZH, Khan WA, Qasim M, Shah IA. MHD stagnation point ferrofluid flow and heat transfer toward a stretching sheet. IEEE Trans Nanotechnol. 2014;13(1):35–40.

[15] Hussanan A, Qasim M, Chen Z-M. Heat transfer enhancement in sodium alginate based magnetic and non-magnetic nanoparticles mixture hybrid nanofluid. Phys A. 2020;550:123957.

[16] Joshi N, Upreti H, Pandey AK, Kumar M. Heat and mass transfer assessment of magnetic hybrid nanofluid flow via bidirectional porous surface with volumetric heat generation. Int J Appl Comput Math. 2021;7:64.

[17] Pandey AK, Upreti H, Joshi N, Uddin Z. Effect of natural convection on 3D MHD flow of MoS_2–GO/H_2O via porous surface due to multiple slip mechanisms. J Taibah Univ Sci. 2022;16(1):749–62.

[18] Tadesse FB, Makinde OD, Enyadene LG. Hydromagnetic stagnation point flow of a magnetite ferrofluid past a convectively heated permeable stretching/shrinking sheet in a Darcy–Forchheimer porous medium. Sādhanā. 2021;46:115.

[19] Tshivhi KS, Makinde OD. Magneto-nanofluid coolants past heated shrinking/stretching surfaces: Dual solutions and stability analysis. Results Eng. 2021;10:100229.

[20] Shafiq A, Lone SA, Sindhu TN, Nonlaopon K. Statistical modelling for the Darcy–Forchheimer flow of Casson cobalt ferrite-water/

ethylene glycol nanofluid under nonlinear radiation. Symmetry. 2022;14:1717.
[21] Usman M, Amin S, Saeed A. Magnetohydrodynamic hybrid nanofluid flow with the effect of Darcy–Forchheimer theory and slip conditions over an exponential stretchable sheet. Adv Mech Eng. 2022;14(8):1–15.
[22] Waini I, Khan U, Zaib A, Ishak A, Pop I, Akkurt N. Time-dependent flow of water-based $CoFe_2O_4$-Mn-$ZnFe_2O_4$ nanoparticles over a shrinking sheet with mass transfer effect in porous media. Nanomaterials. 2022;12:4102.
[23] Tshivhi KS, Makinde OD. Dual solutions and stability analysis for Buongiorno model of magnetohydrodynamics nanofluid flow past a heated shrinking slippery surface. J Nanofluids. 2023;12(6):1485–94.
[24] Murtaza S, Kumam P, Bilal M, Sutthibutpong T, Rujisamphan N, Ahmad Z. Parametric simulation of hybrid nanofluid flow consisting of cobalt ferrite nanoparticles with second-order slip and variable viscosity over an extending surface. Nanotechnol Rev. 2023;12:20220533.
[25] Powell RE, Eyring H. Mechanism for relaxation theory of viscosity. Nat Lond. 1944;154:427–8.
[26] Jalil M, Asghar S, Imran SM. Self similar solutions for the flow and heat transfer of Powell–Eyring fluid over a moving surface in a parallel free stream. Int J Heat Mass Transf. 2013;65:73–9.
[27] Hayat T, Iqbal Z, Qasim M, Obaidat S. Steady flow of an Eyring Powell fluid over a moving surface with convective boundary conditions. Int J Heat Mass Transf. 2012;55:1817–22.
[28] Roşca AV, Pop I. Flow and heat transfer of Powell–Eyring fluid over a shrinking surface in a parallel free stream. Int J Heat Mass Transf. 2014;71:321–7.
[29] Rahimi J, Ganji DD, Khaki M, Hosseinzadeh Kh. Solution of the boundary layer flow of an Eyring-Powell non-Newtonian fluid over a linear stretching sheet by collocation method. Alex Eng J. 2017;56(4):621–7.
[30] Reddy SRR, Reddy PBA, Bhattacharyya K. Effect of nonlinear thermal radiation on 3D magneto slip flow of Eyring-Powell nanofluid flow over a slendering sheet with binary chemical reaction and Arrhenius activation energy. Adv Powder Technol. 2019;30:3203–13.
[31] Abbas W, Megahed AM. Powell-Eyring fluid flow over a stratified sheet through porous medium with thermal radiation and viscous dissipation. AIMS Math. 2021;6(12):13464–79.
[32] Aljabali A, Kasim ARM, Arifin NS, Ariffin NAN, Ching DLC, Waini I, et al. Two-phase flow of Eyring–Powell fluid with temperature dependent viscosity over a vertical stretching sheet. Mathematics. 2022;10:3111.
[33] Tiwari RK, Das MK. Heat transfer augmentation in a two-sided lid-driven differentially heated square cavity utilizing nanofluids. Int J Heat Mass Transf. 2007;50:2002–18.
[34] Patel M, Timol MG. Numerical treatment of Powell-Eyring fluid flow using method of satisfaction of asymptotic boundary conditions (MSABC). Appl Numer Math. 2009;59:2584–92.
[35] Weidman P. Flows induced by power-law stretching surface motion modulated by transverse or orthogonal surface shear. C R Mèc. 2017;345(2):169–76.
[36] Upreti H, Pandey AK, Kumar M, Makinde OD. Ohmic heating and non-uniform heat source/sink roles on 3D Darcy–Forchheimer flow of CNTs nanofluids over a stretching surface. Arab J Sci Eng. 2020;45:7705–17.
[37] Alghamdi M, Wakif A, Thumma T, Khan U, Baleanu D, Rasool G. Significance of variability in magnetic field strength and heat source on the radiative-convective motion of sodium alginate-based nanofluid within a Darcy-Brinkman porous structure bounded vertically by an irregular slender surface. Case Stud Therm Eng. 2021;28:101428.
[38] Sadighi S, Afshar H, Jabbari M, Ashtiani HAD. Heat and mass transfer for MHD nanofluid flow on a porous stretching sheet with prescribed boundary conditions. Case Stud Therm Eng. 2023;49:103345.
[39] Khan U, Zaib A, Pop I, Waini I, Ishak A. MHD flow of a nanofluid due to a nonlinear stretching/shrinking sheet with a convective boundary condition: Tiwari–Das nanofluid model. Int J Numer Methods Heat Fluid Flow. 2022;32(10):3233–58.
[40] Miklavčič M, Wang C. Viscous flow due to a shrinking sheet. Q Appl Math. 2006;64(2):283–90.
[41] Fang T. Boundary layer flow over a shrinking sheet with power-law velocity. Int J Heat Mass Transf. 2008;51(25–26):5838–43.
[42] Merkin JH. Mixed convection boundary layer flow on a vertical surface in a saturated porous medium. J Eng Math. 1980;14(4):301–13.
[43] Weidman PD, Kubitschek DG, Davis AMJ. The effect of transpiration on self-similar boundary layer flow over moving surfaces. Int J Eng Sci. 2006;44(11–12):730–7.
[44] Khan U, Zaib A, Ishak A, Alotaibi AM, Eldin SM, Akkurt N, et al. Stability analysis of buoyancy magneto flow of hybrid nanofluid through a stretchable/shrinkable vertical sheet induced by a micropolar fluid subject to nonlinear heat sink/source. Magnetochemistry. 2022;8(12):188.
[45] Duguma KA, Makinde OD, Enyadene LG. Stability analysis of dual solutions of convective flow of Casson nanofluid past a shrinking/stretching slippery sheet with thermophoresis and Brownian motion in porous media. J Math. 2023;2023:5954860.
[46] Shampine LF, Gladwell I, Thompson S. Solving ODEs with MATLAB. Cambridge: Cambridge University Press; 2003.
[47] Devi SSU, Devi SPA. Heat transfer enhancement of Cu-Al_2O_3/water hybrid nanofluid flow over a stretching sheet. J Niger Math Soc. 2017;36:419–33.
[48] Wang CY. Free convection on a vertical stretching surface. J Appl Math Mech (ZAMM). 1989;69:418–20.
[49] Khan W, Pop I. Boundary-layer flow of a nanofluid past a stretching sheet. Int J Heat Mass Transf. 2010;53:2477–83.
[50] Elatter S, Khan U, Zaib A, Ishak A, Saleh W, Abed AM. Scrutinization of waste discharge concentrations in Eyring-Powell nanofluid past a deformable horizontal plane surface. Water. 2023;15(19):3419.